PAPER

Check for updates

PbV₂O₆ under compression: near zero-linear compressibility and pressure-induced change in vanadium coordination†

Josu Sánchez Martín, [ID] *[a] Julio Pellicer-Porres, [ID] [a] Robin Turnbull, [ID] [a]
Daniel Díaz-Anichtchenko, [ID] [a] Simone Anzellini, [ID] [a] Akun Liang, [ID] [a,b]
Catalin Popescu, [ID] [c] Marco Bettinelli, [ID] [d] Plácida Rodríguez-Hernández, [ID] [e]
Alfonso Muñoz [ID] [e] and Daniel Errandonea [ID] [a]

This study presents evidence that lead metavanadate, PbV₂O₆, is a material with zero-linear compressibility, which maintains its crystal size in one crystallographic direction even under external pressures of up to 20 GPa. The orthorhombic polymorph of PbV₂O₆ (space group *Pnma*) was studied up to 20 GPa using synchrotron powder X-ray diffraction, Raman spectroscopy, and density-functional theory simulations to investigate its structural and vibrational evolution under compression. Up to this pressure we find no evidence of any structural phase transitions by any diagnostic technique, however, a progressive transformation of the coordination polyhedron of vanadium atoms is revealed which results in the zero-linear compressibility. High-pressure Raman experiments enabled the identification and symmetry assignation of all 54 zone-centre Raman-active modes as well as the calculation of their respective pressure coefficients. Three independent high-pressure powder X-ray diffraction experiments were performed using different pressure-transmitting media (Ne, 4 : 1 methanol–ethanol mixture, and silicone oil). The results show a high anisotropic behaviour in the linear compressibility of the crystallographic axes. The PbV₂O₆ bulk modulus of 86.1(9) GPa was determined using a third-order Birch-Murnaghan equation of state. The experimental results are supported by *ab initio* density-functional theory calculations, which provide vibrational patterns, unit-cell parameters, and atomic positions. These calculations also reveal that, unlike MgV₂O₆ and ZnV₂O₆, the band gap of PbV₂O₆ closes with pressure at a rate of −54 meV GPa⁻¹ due to the contribution of the Pb 6s orbital to the top of the valence band.

I. Introduction

The family of metavanadate compounds (MV₂O₆, where M is a divalent atom) exhibits a rich polymorphism, even for each individual M element.[1] The structures that have been most extensively studied are the brannerite-type (space group *C2/m*),[1–3] the columbite-type (space group *Pbcn*)[4,5] and the NiV₂O₆-type (space group *P1̄*).[2,6] It is worth noting that for larger cations, such as Sr, Ba, Hg, or Pb, the metavanadates have orthorhombic structures that differ from those above mentioned.[1]

Lead metavanadate (PbV₂O₆) is known for its magnetic properties[7] and for its use as a catalyst in photoelectrochemical water splitting.[8] PbV₂O₆ has various polymorphs at ambient conditions and normally crystallizes in an orthorhombic structure described by space group *Pnma*, as shown in Fig. 1(a), with *a* = 9.771(10), *b* = 3.684(4), *c* = 12.713(13) Å, and *Z* = 4.[9] In the crystal structure, all atoms are at 4c Wyckoff positions, with V atoms occupying two different positions, V1 and V2. Each V atom is coordinated by 5 oxygen atoms, forming square-based VO₅ pyramids. In the *Pnma* crystal structure of PbV₂O₆, these VO₅ square pyramids share edges to form zig-zag chains parallel to the crystallographic *b*-axis. The alternating pyramids of V1 and V2 are shown in blue and green respectively in Fig. 1(a). The V–O distances within the two VO₅ polyhedra range from 1.610(15) Å to 2.063(15) Å. The next V–O distance is 2.907(14) Å for V1 and 2.619(15) Å for V2. Previous

[a]Departamento de Física Aplicada-ICMUV, Universidad de Valencia, Dr. Moliner 50, 46100 Valencia, Burjassot, Spain. E-mail: Josu.Sanchez@uv.es
[b]Centre for Science at Extreme Conditions and School of Physics and Astronomy, University of Edinburgh, EH9 3FD Edinburgh, UK
[c]CELLS-ALBA Synchrotron Light Facility, Cerdanyola del Vallès, 08290 Barcelona, Spain
[d]Laboratorio Materiali Luminescenti, Dipartimento di Biotecnologie, Università di Verona, and INSTM, UdR Verona, Strada Le Grazie 15, 37134 Verona, Italy
[e]Departamento de Física, MALTA-Consolider Team, Instituto de Materiales y Nanotecnología, Universidad de La Laguna, San Cristóbal de La Laguna, E-38200 Tenerife, Spain
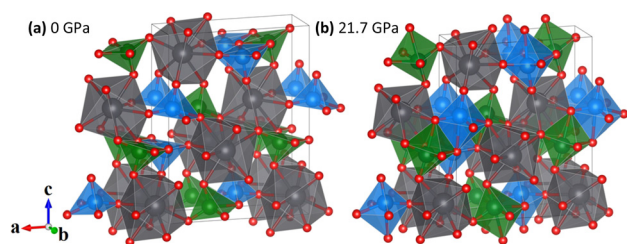†Electronic supplementary information (ESI) available. See DOI: https://doi.org/10.1039/d4dt01321b

Fig. 1 The orthorhombic (*Pnma*) crystal structure of PbV_2O_6. (a) The ambient pressure structure containing VO_5 square pyramids. (b) The structure at 21.7 GPa containing VO_6 octahedra (DFT). The figure illustrates the coordination change of V atoms under HP from 5 to 6. PbO_9 distorted triangular dodecahedra are shown in grey, with oxygen atoms in red. VO_5 square pyramids in (a) and VO_6 distorted octahedra in (b) are shown in blue (V1) and green (V2). The arrows show the crystal axes.

studies have described the structure as being formed by VO_6 octahedra,[9] as in Fig. 1(b). However, due to the long interatomic distance of the largest V–O distance, it cannot be considered a proper bond. Instead, it is more actually described as a secondary intermolecular bond, which could be easily modified under compression.[10]

We will demonstrate here that VO_6 configuration is only achieved under compression. Each VO_5 polyhedron corner-shares *via* oxygen atoms with the PbO_9 distorted triangular dodecahedra. Each one of the nine oxygen atoms in the PbO_9 polyhedron comes from a different VO_5 pyramid. The PbO_9 polyhedron has eight Pb–O bonds with distances from 2.562(12) Å to 2.703(10) Å plus a long bond with a distance of 2.996(15) Å. The PbO_9 polyhedra form Pb_2O_{16} dimers *via* edge sharing. In addition to the stable polymorph of PbV_2O_6, two metastable polymorphs can be synthesized *via* quenching of the melt: $PbV_2O_6(\text{II})$, which has the brannerite-type structure,[11] and $PbV_2O_6(\text{III})$ which crystallizes in an orthorhombic structure (space group $C222$) and is isostructural to SrV_2O_6.[12]

Metavanadates exhibit a wide variety of polymorphs, each with distinct a behaviour under high-pressure (HP), which has attracted the interest of various research groups. Even though they present different crystal structures and vanadium coordination compared to the square pyramid VO_5 coordination of PbV_2O_6, to put our research in context, it is worth taking a look to the whole picture of what has been done in this vanadate family. For instance, SrV_2O_6 and BaV_2O_6 (orthorhombic space group $C222$) undergo phase transitions at about 4 GPa, followed by amorphization between 9 and 10 GPa.[13] At pressures above 19 GPa, the brannerite-type MgV_2O_6 undergoes a phase transition to a structure described by space group $C2$,[14] while the columbite-type remains stable up to 22 GPa.[15] For ZnV_2O_6, a density-functional theory (DFT) study was conducted considering twelve different potential polymorphs up to 30 GPa, finding that only four of them do not have imaginary phonons, and that under compression the brannerite-type might have a transition first to the columbite-type structure at 5 GPa, and then to the monoclinic $ThTi_2O_6$-type structure at 15 GPa.[16] This same brannerite-type ZnV_2O_6 was subsequently

studied by X-ray diffraction, contradicting the DFT predictions and finding a phase transition to a monoclinic structure (space group $C2$) at 16.6 GPa.[17,18]

This work presents a combined experimental and computational study of PbV_2O_6 up to 20 GPa, including vibrational and structural analysis. Raman spectroscopy was used to determine the frequency and symmetry assignment of all 54 vibrational modes under both ambient and HP conditions. Additionally, powder X-ray diffraction (XRD) data were collected using three different pressure-transmitting media (PTM) in order to determine the unit-cell parameters as a function of pressure. The results indicate that PbV_2O_6 remains in the low-pressure orthorhombic phase under compression up to 20 GPa. However, we also found evidence of a pressure-induced change in the coordination environment of vanadium. From the XRD data, we have calculated the bulk modulus (B_0) and the linear compressibilities of the three crystallographic axes. We found that PbV_2O_6 has a zero linear compressibility along the *b*-axis, making it suitable for a wide range of potential applications in complex extreme environments. DFT calculations support all mentioned measurements. They also add the expected infrared (IR) active modes and their pressure coefficients, which have not yet been reported in the literature. The DFT simulations also provide information on the band structure and pressure dependence of the band-gap energy.

II. Methods

A. Synthesis

Orthorhombic PbV_2O_6 was synthesized *via* a solid-state reaction.[9] High-purity PbO (99.9% Alfa Aesar) and V_2O_5 (Carlo Erba 99%) were mixed in a 1:1 stoichiometric ratio and transferred to a Pt crucible with a tightly fitting lid. The mixture was heated in a horizontal furnace in an air atmosphere, starting from room temperature and increasing at a constant rate to 650 °C for one hour, and then maintained at this temperature for 15 minutes. The furnace was then switched off and allowed to cool down to 220 °C. Subsequently, the crucible was removed from the furnace and left to cool to room temperature. The resulting sample was extracted mechanically from the container and washed with doubly distilled water. The obtained powder exhibited a brown-black colour. The orthorhombic crystal structure of PbV_2O_6 was confirmed by powder XRD.

B. Details of high-pressure experiments

Raman spectra were acquired in the backscattering geometry using a 632.8 nm He–Ne laser and a Jobin–Yvon spectrometer combined with a thermoelectric-cooled multichannel CCD detector with a spectral resolution of 2 cm^{-1}. OptiGrate Volume Bragg gratings were used to be able to filter the laser from around 10 cm^{-1}. A low laser power of around 2 mW was used to avoid damaging the sample due to heating. The samples were loaded into a diamond-anvil cell (DAC) equipped with low fluorescence diamonds of 350 μm of culet, along with a ruby chip and a stainless-steel gasket. Sample and ruby were embedded in Ne

pressure-transmitting medium (PTM) to ensure good hydrostatic conditions.[19] The pressure inside the DAC was determined using the ruby luminescence method following the calibration of ref. 20. The Raman mode fitting was performed with MATLAB[21] assuming a Pseudo-Voigt peak profile.

We performed three sets of HP powder XRD measurements using the same DAC as in the Raman experiment, where the PTM loaded was different in each run: Ne, 4 : 1 methanol–ethanol mixture (ME), and silicone oil (SilOil). All XRD experiments were conducted at the MSPD beamline of the ALBA synchrotron[22] using a monochromatic beam of wavelength 0.4246 Å (Ne and ME) and 0.4642 Å (SilOil). The use of different PTM was motivated to check the influence of non-hydrostatic stresses in the behaviour of PbV_2O_6 under compression. The X-ray beam was focused down to a 20 μm × 20 μm full width at half maximum (FWHM). A Rayonix charge-coupled device detector was used to collect the XRD patterns, with a sample-to-detector distance of 300 (Ne and ME) or 280 mm (SilOil), calibrated following standard procedure using the XRD pattern obtained from LaB_6 standard. The pressure was determined using the XRD reflections and the equation of state (EOS) of Cu[23] with a precision of ±0.1 GPa. The collected XRD were transformed into one-dimensional patterns using DIOPTAS[24] and the structural analysis was performed with PowderCell.[25]

C. *Ab initio* density-functional theory calculations

In this study, zero-temperature simulations were performed with the well-known plane-wave pseudopotential method in the framework of the density-functional theory[26] implemented in the Vienna *Ab initio* Simulation Package, VASP.[27] The projector augmented wave (PAW) pseudopotentials[28,29] provided in the VASP pseudopotentials database were used, and the exchange–correlation term was described by the generalized gradient approximation (GGA), using the AM05[30,31] functional. The Brillouin zone k-points sampling was performed with a Monkhorst–Pack[32] sampling of 4 × 8 × 4 for the primitive cell. A plane-wave basis set with an energy cutoff of 600 eV was employed to ensure accurate and highly converged results. All degrees of freedom, lattice parameters, and internal atomic parameters were fully relaxed with self-consistent convergence criteria of 10^{-6} eV, below 0.003 eV Å^{-1}, and 0.1 GPa, for the total energy, atomic forces, and stress tensor deviation from a diagonal hydrostatic form, respectively. From our simulations, we obtain a set of volume, energy, and pressure data that can be fitted with a Birch–Murnaghan[33] equation of state. To analyse the vibrational characteristics, the Phonopy package[34] was utilized. The normal mode frequencies and associated eigenvectors were determined at the Γ-point.

III. Results and discussion

A. High pressure Raman spectroscopy

With four molecules in the primitive unit cell, PbV_2O_6 has a total of 108 vibrational modes. Symmetry analysis shows that

all 54 even modes are Raman active,[35] $\Gamma_{\text{Raman}} = 18A_g + 9B_{1g} + 18B_{2g} + 9B_{3g}$. By utilizing the information provided by the DFT calculations and the pressure-dependent evolution of modes of the Raman spectra, we have identified the 54 Raman-active modes along with their corresponding symmetries at ambient conditions, as shown in Fig. 2. The figure shows that the symmetry of the modes is mostly distributed in pairs with the same ordering number (superscript). For example, the A^4_g and B^4_{2g} modes are close together, as are the B^3_{1g} and B^3_{3g} modes. Several B_{1g} and B_{3g} overlap (identified with violet colour in Fig. 2), in which case a single Raman peak is assigned to both modes. Comparing A_g and B_{2g} modes, the intensity of A_g modes is usually larger. Small or partially hidden modes, such as B^2_{2g} or A^{14}_g, are fitted in Fig. 2 as they were properly found in spectra under compression, as their contribution increased in intensity, or they were no longer overlapped by other modes.

Regarding the evolution of the Raman spectra under compression, all modes were observed to shift towards higher wavenumbers with increasing pressure, as shown in Fig. 3. No evidence of phase transition was detected in Raman experiments. From this analysis only 48 out of the 52 modes could be followed under compression due to mode overlap. As pressure was increased two interesting phenomena were observed. Firstly, a significant increase in the intensity of the modes above 800 cm^{-1} occurs starting from 3.9(1) GPa. These modes involve significant stretching movements of the V–O bonds.[4,16,36] Therefore, it is not surprising that they will be affected by changes the coordination polyhedron of V that we determined based on XRD experiments and DFT calculations. This observation is discussed in detail in section III.B. Secondly, the intensity of the Raman signal decreases with
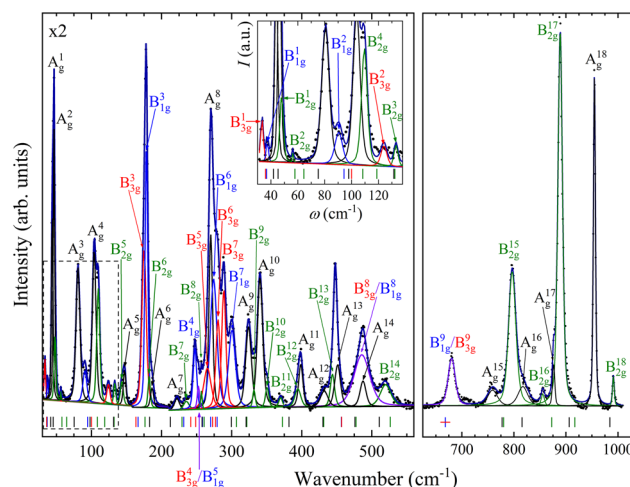

Fig. 2 Raman spectrum of PbV_2O_6 at 0.5(1) GPa showing the assigned mode symmetries. The vertical ticks represent the positions of the Raman modes according to the DFT calculations. The colour of the tick marks corresponds to the symmetry of the respective Raman mode. Violet colour is used when red and blue overlap. The inset corresponds to the dashed area. Magnification of the first region is shown in the top left corner.
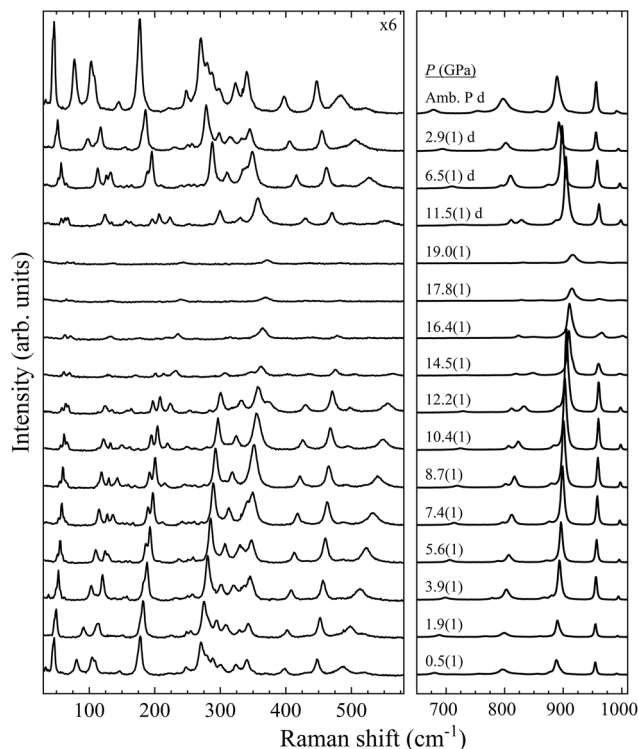
Fig. 3 High pressure PbV_2O_6 Raman spectra at selected pressures. The numbers next to the spectra indicate the pressure in GPa. Spectra acquired on decompression are marked with the letter "d".

increasing pressure from 14.5(1) GPa up to the maximum pressure achieved, 19.0(1) GPa, making impossible to distinguish some of the weaker modes from the background. We consider that this phenomenon could be related to absorption of the excitation laser by the sample[37] caused by the decrease of the band-gap energy of PbV_2O_6 under compression. The band-gap energy at ambient pressure is 2.6 eV (ref. 8) and it is a well-known effect that in lead oxides the bandgap closes under compression at a rate between −43 and −72 meV GPa^{-1}.[38–40] According to our DFT calculations in PbV_2O_6 the band gap closes linearly with a rate of −54 meV GPa^{-1}. Therefore, it would not be surprising that near 14.5 GPa the band-gap energy would be around 1.95 eV (683 nm), below the energy of the excitation laser, with the consequent decrease of Raman intensity. This hypothesis is consistent with the fact that the observed signal loss is reversible. The aforementioned pressure induced shift of the Raman modes and increase in intensity of the V–O vibrational modes above 3.9(1) GPa are also totally reversible upon decompression. Comparing PbV_2O_6 to other metavanadates, it shares the same stability range as the brannerite-type MgV_2O_6[14] and ZnV_2O_6,[17,18] which suggest that these structures are more stable than those of SrV_2O_6 and BaV_2O_6.[13] The difference in pressure stabilities could be related to the more open structural framework of the alkaline rare-earth metavanadates. However, the experiments on SrV_2O_6 and BaV_2O_6 should be repeated. For example, the Raman modes reported in ref. 13 become overly broad at low

pressures, suggesting a possible bridging of sample between the diamond anvils, which could largely reduce transition pressures[41] and trigger amorphization.

In Table S1 of the ESI† we report the wavenumbers of all Raman-active modes at ambient conditions and their pressure coefficients obtained from experiments and calculations. The level of agreement between the experiments and calculations is relatively high. In the case of the pressure coefficients, a few modes (B^1_{1g}, B^2_{2g}, B^4_{1g}, A^9_g, B^9_{2g}, and B^{11}_{2g}) have differing values, but they are low intensity peaks which are difficult to follow under pressure. A^8_g represents the only exception, being easily measured but presenting less than half of the expected pressure coefficient. Furthermore, we show in Fig. 4 and 5 the evolution of all experimentally measured modes along with results from DFT calculations. In Fig. 4 it can be seen a change in the behaviour of the B^7_{1g} and B^7_{3g} modes around 11–12 GPa. These are bending vibrations of V–O bonds. It is not surprising that changes in the V coordination would affect their pressure dependence. DFT was key for assigning the symmetry of Raman modes enabling comparison not only of the ambient pressure values, but also of the pressure evolution and the mode crossings. We did not detect any Raman mode of the impurities mentioned in section III.B.

The DFT calculations also provided the forty-two infrared (IR) active modes, all with B_{1u}, B_{2u}, and B_{3u} symmetry, which is the same symmetry of the three acoustic modes. There are nine remaining modes with A_u symmetry which are silent. The wavenumbers and pressure coefficients of the IR active modes in ambient conditions are given in Table S2.†
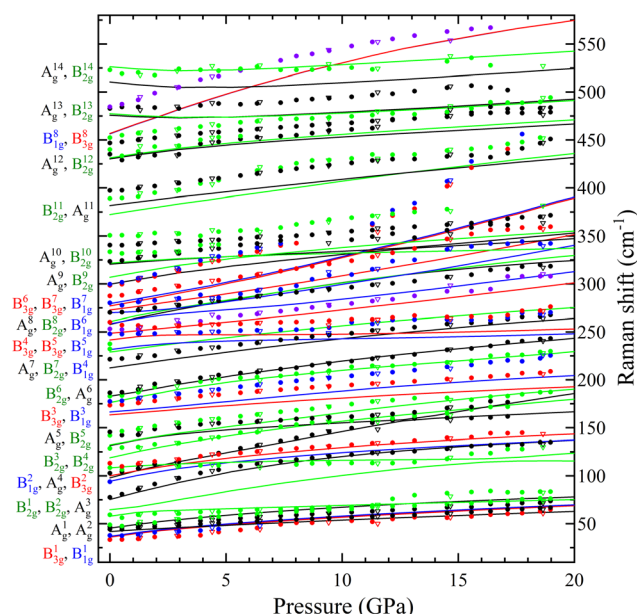

Fig. 4 Pressure dependence of the Raman modes from 10 to 580 cm^{-1} of PbV_2O_6. Solid circles (empty triangles) correspond to data acquired on sample (de)compression. The colours of the symbols and lines match with the mode symmetries assigned shown to the left-hand side of the graph. Solid lines are from DFT calculations. Violet colour is used when red and blue overlap.
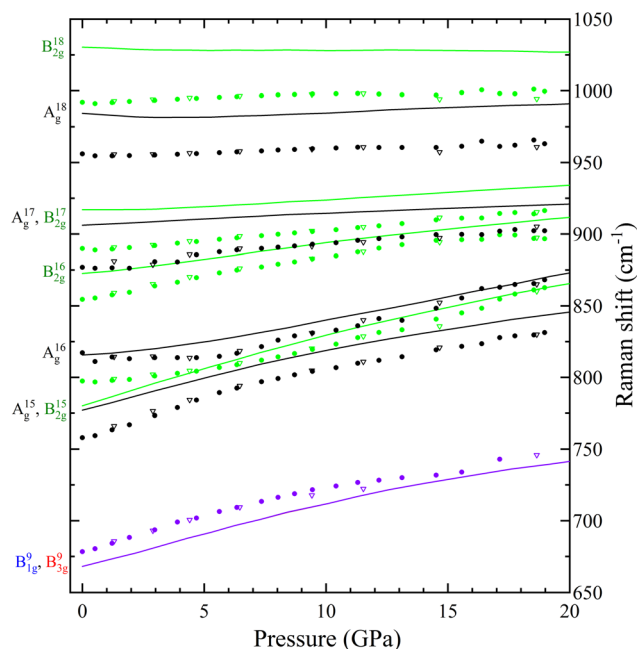
Fig. 5 Pressure dependence of the Raman modes from 650 to 1050 cm^{-1} of PbV$_2$O$_6$. Solid circles (empty triangles) correspond to data acquired on sample (de)compression. The colours of the symbols and lines match with the mode symmetries assigned shown to the left-hand side of the graph. Solid lines are from DFT calculations. Violet colour is used when red and blue overlap.

B. High pressure X-ray diffraction

Three independent HP powder XRD experiments were performed on PbV$_2$O$_6$ using three different pressure transmitting media (Ne, ME, and SilOil), reaching a maximum pressure of around 20 GPa in all three runs. Due the influence of preferred orientation effects in the XRD patterns, the Le Bail refinement technique[42] was used to analyse the data from all the XRD experiments. The Le Bail fits are shown in Fig. 6 for each PTM at selected pressures. The orthorhombic ambient-pressure structure was successfully fitted in all diffractograms, but additional weak peaks were also detected which have been assigned to rutile-type β-PbO$_2$ (space group $P4_2/mnm$) and V$_2$O$_5$ (space group $Pmn2_1$). As the peaks of the impurities did not overlap significantly with the peaks from the sample, their presence does not affect the analysis. Additionally, we also observed that the impurity peaks gradually disappeared as pressure was increased and were absent during decompression (see Fig. 6a and b). The disappearance of the V$_2$O$_5$ peaks may be attributed to its well-known pressure-induced irreversible amorphization.[43] In the case of β-PbO$_2$, it is known that no phase transition occurs up to 20 GPa.[44] However, XRD peaks have been found to broaden due to a pressure-induced disorder of the crystal structure.[44] This phenomenon could account for the disappearance of the weak peaks associated with the β-PbO$_2$ impurities.

In all three experiments, XRD patterns are consistent with the ambient-pressure orthorhombic structure of PbV$_2$O$_6$

described by space group $Pnma$, as shown in Fig. 6 where we include R-values from the fits. In the case of the ME and SilOil experiments the peak matching above 15 GPa is not as good as in the other experiments probably due to the influence of non-hydrostatic stresses. Interestingly, during the experiment performed using ME as PTM, we noticed a significant and counterintuitive observation. Beyond 10 GPa, there are XRD reflections, particularly those with a Miller index where $k \neq 0$, that evolve with pressure to lower angles. For instance, the arrows over the (011) and (111) reflections in Fig. 6b show this effect. This shift in diffraction peaks towards lower angles indicates an increase in interplanar spacing under sample compression, contrary to the usual observation of a pressure-induced decrease in interplanar spacing. This effect motivated us to repeat the experiment using different PTM to check if the observed phenomenon could be related to non-hydrostatic effects, which begin to develop in ME at 10 GPa.[19] Therefore, we performed subsequent experiments using Ne, a quasi-hydrostatic PTM in the pressure range of experiments, and SilOil, a PTM where non-hydrostatic contributions develop beyond 4 GPa.[19,45] These results confirmed the influence of non-hydrostatic stresses in the HP behaviour of PbV$_2$O$_6$. Fig. 6a shows that in the Ne experiment, all peaks move towards higher angles with increasing pressure. In contrast, in the SilOil experiment (Fig. 6c), the peaks move towards lower angles, as in the ME experiment (Fig. 6b). As explained below, the counterintuitive shift of the diffraction peaks with a Miller index of $k \neq 0$ is due to an artificial expansion of the b-axis caused by the Poisson effect. This is consistent with the structural framework of the PbV$_2$O$_6$ crystal structure. Fig. 1 shows that the b-axis is the shortest of the three axes and that polyhedral chains are aligned along this axis. Consequently, the b-axis is expected to be the least compressible. Under non-hydrostatic conditions, the expansion of this axis is due to deviatoric stresses along the perpendicular directions.[46]

The unit-cell lattice parameters and volume of PbV$_2$O$_6$ were obtained from the XRD data of three experiments conducted from ambient conditions up to 20 GPa. The results are shown in Fig. 7 together with results from DFT calculations. These calculations agree with experiments at ambient pressure, with only a 1% underestimation of the parameter b. These data sets were used to compute the linear compressibility and the $P–V$ equation of state (EOS) for the room-temperature isotherm. Fig. 7 clearly shows the effect of deviatoric stresses on the structure of PbV$_2$O$_6$. According to Ne experiments and DFT calculations the parameters a and c are considerably more compressible than the parameter b. In addition, there is a decrease of the compressibility of b at 15 GPa, with the slope becoming nearly zero beyond this pressure. In both ME and SilOil experiments, a change in the sign of the slope of the pressure dependence of the parameter b occurs at 10 GPa, with b increasing under compression for higher pressures. This phenomenon is more pronounced in the SilOil experiment. Additionally, in the SilOil experiment, the compressibility of the parameter a also decreases at 3 GPa, becoming smaller than the compressibility observed in the other two experiments. The pressure depen-
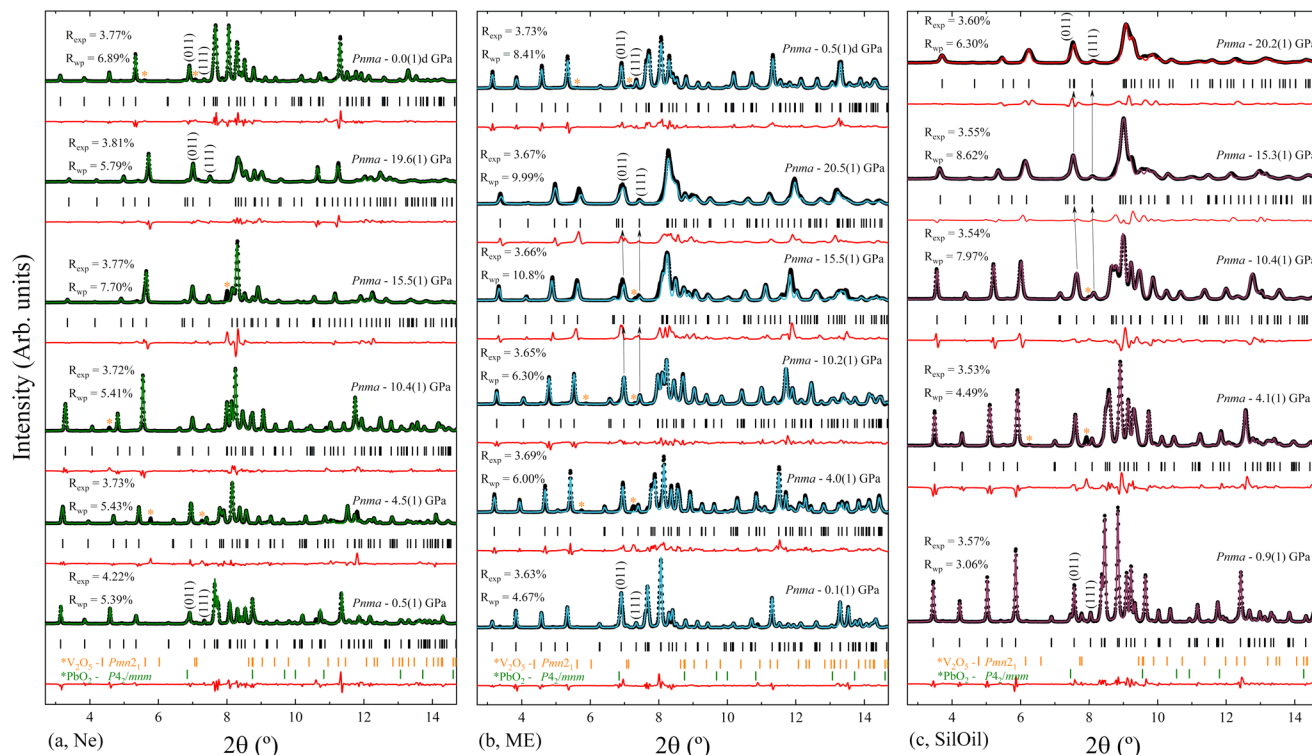
Fig. 6 XRD patterns and corresponding Le Bail fits of PbV_2O_6 at selected pressures. Le Bail fits are shown with green (a, Ne), blue (b, ME) and pink (c, SilOil) lines, while residuals are shown with red lines. Experimental data are shown with black symbols. Vertical ticks indicate the Bragg reflections for the corresponding structural phase. (Impurities are considered only in the first spectrum and marked in the rest with asterisks.) Pressures are indicated in the figure. The top trace corresponds to the last data acquired during decompression for (a, Ne) and (b, Me). Arrows in (b, Me) and (c, SilOil) highlight examples of reflections shifting to lower values of 2θ as pressure increases.

dence of the volume reveals more noticeable changes, as the results from the SilOil (ME) experiment differ from those obtained from the Ne experiment and DFT simulations at 3.2 (1) GPa. These pressures coincide with those where the two PTM become non-hydrostatic.[19] This indicates that PbV_2O_6, and likely related compounds, is significantly affected by non-hydrostatic stresses.

To analyse the pressure dependence of the volume, we determined a P–V EOS using DFT calculations and data from each experiment conducted within the hydrostatic range of the PTM. We used a second-order Birch-Murnaghan EOS[33] employing the EosFit7 software.[47] The second order nature of the EOS was confirmed from the Eulerian strain-normalized pressure dependence of the data (see Fig. S1 in the ESI†).[48] The EOS parameters are summarized in Table 1. Overall, the experimental and calculated results show exceptional agreement, particularly for the Ne run, in which the PbV_2O_6 bulk modulus was determined to be 86.1(9) GPa. Other published metavanadates exhibit significantly higher bulk moduli, including 188(5) GPa for MgV_2O_6[14] and 147(2) GPa for ZnV_2O_6,[18] which crystallize in the brannerite-type structure. This difference may be connected to the fact that the Pb–O bonds, which are more compressible than the Mg–O and Zn–O bonds. These bonds are expected to dominate the volume change of the metavanadates.[18] This hypothesis is consistent

with the fact that the sequence of bulk moduli PbV_2O_6 < ZnV_2O_6 < MgV_2O_6 is the same as in the compounds PbO < ZnO < MgO.[49–51]

The linear isothermal compressibility for all crystallographic axes of the orthorhombic structure was obtained using the online PASCal tool.[52] Data up to 1.5 GPa was used to guarantee hydrostatic conditions for all PTM used. The obtained linear compressibilities at 0 GPa are $\kappa_a = 4.0(5) \times 10^{-3}$ GPa^{-1}, $\kappa_b = 1.6(2) \times 10^{-3}$ GPa^{-1} and $\kappa_c = 8.0(7) \times 10^{-3}$ GPa^{-1} according to the experiments and $\kappa_a = 2.87(4) \times 10^{-3}$ GPa^{-1}, $\kappa_b = 1.12(2) \times 10^{-3}$ GPa^{-1} and $\kappa_c = 8.20(7) \times 10^{-3}$ GPa^{-1} from the DFT results. As expected, the b axis is less compressible than the other two unit-cell axes, showing a near zero linear compressibility, with is similar to that of diamond, 0.7×10^{-3} GPa^{-1},[53] and comparable to that of $Li_2Ti(IO_3)_6$, the record zero-linear compressibility material.[54] This makes PbV_2O_6 an excellent candidate for shock-resistant and protection coatings for components of aviation working under extreme conditions.[55]

Since calculations show a good agreement with experiments results regarding the pressure dependence of unit-cell parameters and phonon frequencies, and Rietveld refinements could not be performed due to preferred orientations effects, we used the DFT calculated atom positions to analyse the evolution of the constituent polyhedra and corresponding bond lengths in the crystal structure under pressure. Such approach
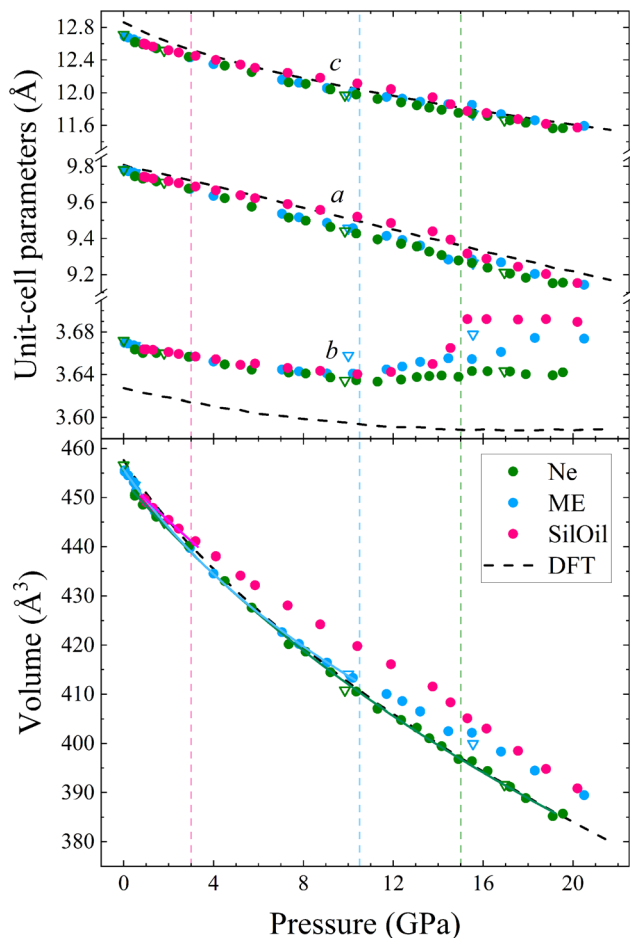
Fig. 7 Pressure dependence of the unit-cell parameters (top) and volume (bottom) of PbV_2O_6. Green, blue and pink symbols represent experimental measurements using Ne, ME and SilOil (respectively) as PTM. Black dashed lines are from DFT calculations. Solid circles (empty triangles) represent data acquired on sample (de)compression. Hydrostatic limits of the corresponding pressure transmitting media are shown with vertical dashed lines. Solid lines are the Birch-Murnaghan EOS fits of the experimental unit-cell volume up to 3.2(1) GPa for Silicon Oil, up to 10.2(1) GPa for ME and up to 19.6(1) GPa for Ne. Error bars are smaller than symbols.

Table 1 EOS parameters (cell volume per formula unit, bulk modulus, and its first derivative) for PbV_2O_6 obtained through the fitting of second order Birch-Murnaghan model (B'_0 is fixed at 4)

PbV_2O_6	V_0 ($Å^3$)	B_0 (GPa)
Ne PTM up to 19.6(1) GPa	453.4(5)	86.1(9)
ME PTM up to 10.2(1) GPa	454.7(4)	85.6(16)
Silicon oil PTM up to 3.2(1) GPa	454.1(4)	98(5)
DFT calculations up to 21.7 GPa	455.70(19)	82.6(4)

has been successfully used in the past for understanding related ternary oxides.[56] To analyse the pressure-evolution of the polyhedral units, we compare the intermolecular V–O bond which connects neighbouring VO_5 polyhedra (dashed line in Fig. 8) with the average V–O bond length within the
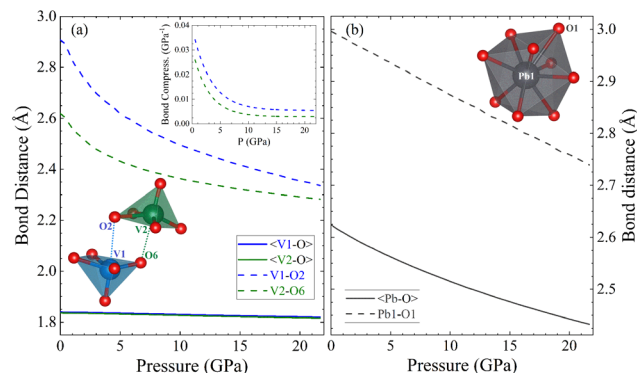

Fig. 8 Pressure evolution of V–O (a) and Pb–O (b) bond distances in PbV_2O_6 as determined by density functional theory calculations. The average bond distances (solid lines) do not account for the longest bond in the polyhedron (dashed line). In the case of vanadium, the longest V–O bond is the intermolecular bond shown as a dotted line in the lower inset in part (a). The upper inset shows the compressibility of the longest V–O bond as a function of pressure.

VO_5 unit, and the longest Pb–O bond of the PbO_9 polyhedron with the average Pb–O bond length within the same polyhedron. The results are shown in Fig. 8. As shown in Fig. 8(a), the intermolecular V–O bonds (dashed lines) are highly compressible, with the average bond distance within the VO_5 polyhedra remaining essentially unchanged under pressure. The second observation is consistent with the fact that V–O covalent bonds are highly incompressible.[57] The first observation shows that the intermolecular V–O bond attains compressibilities comparable to that of covalent bonds between 5 and 10 GPa (see inset in Fig. 8(a)).[58] The development of the sixth V–O bond is supported by the calculated electron-localization function shown in Fig. S2 in the ESI.† The determination of the nature of this bond requests the performance of crystal orbital Hamilton population calculations which is beyond the scope of this study. The formation of a sixth V–O bond leads to the conversion of all the VO_5 pyramids into VO_6 octahedra, thereby forming rigid columns of edge-sharing VO_6 octahedra along the *b*-direction (see Fig. 1(b)). This rigid column of VO_6 octahedra is what makes the *b*-axis incompressible beyond 15 GPa. Regarding the PbO_9 polyhedron, we found that the longest Pb–O bond is equally as compressible as the others in the polyhedron (see Fig. 8(b)). Fig. 8 shows that the Pb–O bonds are much more compressible than the V–O bonds. In contrast, the long and weak sixth V–O bond is much more compressible up to 5 GPa, where the compressibility becomes similar to that of Pb–O bonds. The compressibility of the sixth V–O bond is shown in the inset of Fig. 8(a). At low-pressure, its values are comparable to the compressibility of weak halogen bonds.[59] The pressure dependence of the long V–O bond resembles an exponential decay, with the compressibility becoming nearly identical to that of Pb–O bonds ($4.5 × 10^{-3}$ GPa^{-1}) around 5 GPa. This observation supports the idea that, under ambient conditions, vanadium atoms form rigid VO_5 polyhedra which are linked to each other *via* weak secondary

V–O bonds. The compressibility and behaviour of this bond support the formation of a sixth V–O bond at around 5 GPa. This phenomenon is consistent with the increase in signal of the Raman-active modes at similar pressures, which we believe it is related to the configurational changes of the coordination polyhedra of vanadium and behaviour of this bond support the formation of a sixth V–O bond at around 5 GPa. This phenomenon is consistent with the increase in signal of the Raman-active modes at similar pressures, which we believe it is related to the configurational changes of the coordination polyhedra of vanadium.

To conclude this section, we will use polyhedral compressibility to better understand pressure-induced changes in the volume. Fig. 9 shows the normalized volume of the unit-cell compared with the normalized volume of different polyhedra, with VO_6 octahedra considered for all pressures. The figure indicates that the PbO_9 polyhedra undergo the majority of the volume reduction, particularly from 5 GPa onwards. In addition, the PbO_9 distortion index, calculated using the formula proposed by Baur,[60] is shown in the inset of Fig. 9. It demonstrates that the shape of PbO_9 polyhedra remains regular under compression. In contrast, the VO_6 octahedra gain symmetry as pressure increases, despite being slightly compressible due to the decrease in the long V–O distance. This confirms the hypothesis that the compressibility of PbV_2O_6 is determined by the Pb polyhedron.
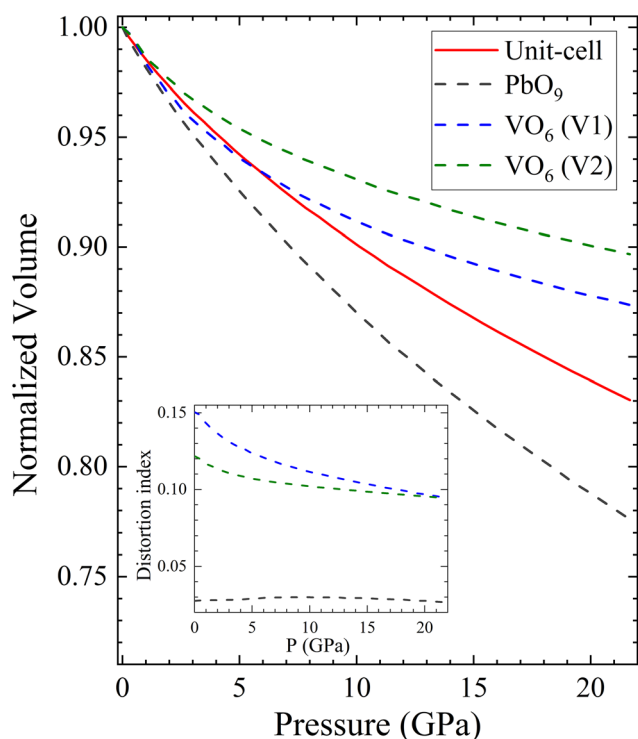
C. Band structure and band gap

In Fig. 10 we report the calculated band structure of PbV_2O_6 at 0 and 20 GPa and the corresponding electronic density of states. At 0 GPa, the valence band maximum is at the Γ-point of the Brillouin zone (BZ), which the conduction band has three nearly degenerate minima. The lowest is at the Y point of the BZ, and the other two are at Γ and T. The calculated band-gap energy is 1.98 eV, which underestimates the bandgap by 0.6 eV according to ref. 9, which is typical of the GGA when using the PBEsol functional. The electronic density of states indicates that the states at the top of the valence band mainly originate from the O 2p orbitals, with a non-negligible contribution of Pb 6s orbitals. The bottom of the conduction bands mainly consists of contributions from the V 3d and O 2p orbitals, with the V 3d orbital contributing the most. The contribution of Pb 6s states to the valence band explains why PbV_2O_6 has a bandgap 0.5 eV smaller than that of MgV_2O_6 and ZnV_2O_6,[16,18] where the states near the Fermi level are only contributed to by the V 3d and O 2p orbitals. This behaviour has also been observed in other ternary oxides when Pb is the divalent cation instead of Cd, Zn, or an alkaline-earth metal.[38–40]

As pressure increase, several changes are observed. Firstly, the bandgap closes, reaching a value of 0.88 eV at 20 GPa. This closure follows a linear dependence with pressure, with a slope -54 meV GPa^{-1}. Additionally, there is a noticeable change in the topology of the band structure, which becomes more dispersive. Consequently, at 20 GPa, PbV_2O_6 becomes a direct gap material with the bandgap located at the Γ point of the BZ. At this pressure, the conduction band has two additional minima close in energy to the minimum at the Γ point, located at the T and Z points. The closing of the bandgap is due to the enhancement of the contribution of Pb
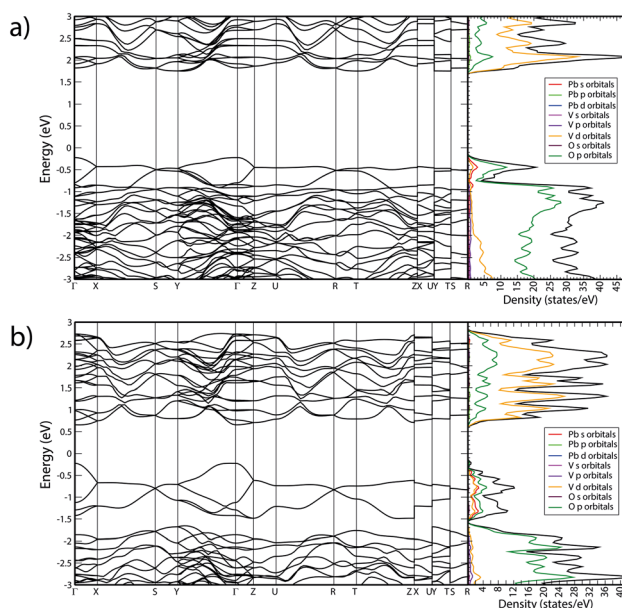

Fig. 9 Pressure evolution of the calculated normalized volume of the PbV_2O_6 unit-cell (solid red line) and the different internal polyhedra (dashed lines). The inset shows how the distortion index of each polyhedra changes under pressure.

Fig. 10 Calculated band structure and electronic density of states of PbV_2O_6 at (a) 0 GPa and (b) 20 GPa.

6s states to the top of the valence band, which is a distinctive feature of the presence of lead atoms. This contrasts with the behaviour of MgV_2O_6 and ZnV_2O_6,[16,17] where the bandgap is determined by V 3d and O 2p states, and it is little affected by pressure. To conclude we would like to add that the closing of the band-gap predicted by DFT (and supported by the decrease of Raman signal) could not be confirmed by absorbance measurements because we have a powder sample, and such studies request single crystals. We hope our predictions will trigger the synthesis of PbV_2O_6 single crystal and the performance of HP optical-absorption experiments.

IV. Conclusions

The study investigated the structural and vibrational evolution of PbV_2O_6 under compression up to 20 GPa using synchrotron powder X-ray diffraction, Raman spectroscopy and density-functional theory simulations. The ambient pressure ortho-rhombic structure (space group *Pnma*) remained stable over the whole pressure range; however, it exhibited a zero-linear compressibility along the *b*-axis comparable to that of diamond. The study determined the wavenumbers and symmetries of 54 zone-centre Raman-active modes at ambient conditions, which were previously uncharacterized. Subsequently 48 of these modes were studied under compression in order to determine their respective pressure coefficients. HP angle dispersive powder XRD analysis was performed using three different PTM (Ne, ME, and SilOil) determined that PbV_2O_6 is highly affected by non-hydrostatic effects. The linear compressibility of each axis and EOS parameters, including bulk moduli, are reported. All experimental results were supported by DFT calculations, finding exceptional agreement among all sets of data. The DFT simulations also provide information on the pressure dependence of IR modes and the electronic band structure of PbV_2O_6, offering more insight into the behaviour of the vanadium–oxygen bond behaviour under pressure. An analysis of bond distances reveals that compression leads to a transformation of the coordination environment of vanadium. At approximately 5 GPa, a secondary intermolecular V–O bond is transformed into an intermolecular bond. This results in the conversion of the VO_5 pyramids into edge sharing VO_6 octahedra, which are aligned along the *b* axis. This phenomenon explains the exceptionally low compressibility observed in that crystallographic direction in PbV_2O_6. Finally, it was found that pressure causes a significant decrease in the band gap due. This is due to the contribution of Pb 6s states to the bottom of the conduction band.

Author contributions

J. Sánchez-Martín and J. Pellicer-Porres were involved in the HP Raman experiments. J. Sánchez-Martín, R. Turnbull, D. Díaz-Anichtchenko, S. Anzellini, A. Liang, C. Popescu and D. Errandonea were involved in the HP XRD measurements. J. Sánchez-Martín, J. Pellicer-Porres, and D. Errandonea were involved in the data analysis. M. Bettinelli was involved in the sample synthesis. P. Rodríguez-Hernández and A. Muñoz were involved in the DFT calculations. The manuscript was written through contributions of all authors. All authors have given approval to the final version of the manuscript.

Data availability

All relevant data are available from the corresponding author upon reasonable request.

Conflicts of interest

There are no conflicts to declare.

Acknowledgements

References

1. P. Garnier and D. Weigel, *J. Solid State Chem.*, 1983, **47**, 16.
2. H. Müller-Buschbaum and M. Kobel, *J. Alloys Compd.*, 1991, **176**, 39.
3. M. S. Islam, H. Kabir, Y. Inagaki and A. R. Sarker, *J. Alloys Compd.*, 2020, **829**, 154499.
4. J. P. Peña, P. Bouvier, M. Hneda, C. Goujon and O. Isnard, *J. Phys. Chem. Solids*, 2021, **154**, 110034.
5. M. Gondrand, A. Collomb, J. C. Joubert and R. D. Shannon, *J. Solid State Chem.*, 1974, **11**, 1.
6. G. M. Clark and A. N. Pick, *J. Therm. Anal.*, 1975, **7**, 289.
7. E. Agostinelli, P. Filaci, D. Fiokani, A. Montenero and M. Bettinelli, *J. Non-Cryst. Solids*, 1986, **84**, 329.

8   S. S. Kalanur, Y. J. Lee and H. Seo, *ACS Appl. Mater. Interfaces*, 2021, **13**, 25906.

9   B. D. Jordan and C. Calvo, *Can. J. Chem.*, 1974, **52**, 2701.

10 R. Turnbull, J. Sánchez-Martín, R. Oliva, J. Ibáñez, C. Popescu, P. Rodríguez-Hernández, A. Muñoz, G. Nénert, D. Vie and D. Errandonea, *Phys. Rev. Mater.*, 2023, **7**, 084606.

11 G. Calestani, G. D. Andreetti and A. Montenero, *Acta Crystallogr., Sect. B: Struct. Sci.*, 1985, **41**, 177.

12 G. Calestani, G. D. Andreetti and A. Montenero, *Acta Crystallogr., Sect. B: Struct. Sci.*, 1985, **41**, 179.

13 Y. Li, R. Tang, N. Li, H. Li, X. Zhao, P. Zhu and X. Wang, *J. Appl. Phys.*, 2015, **118**, 035902.

14 R. L. Tang, Y. Li, Q. Tao, N. N. Li, H. Li, D. D. Han, P. W. Zhu and X. Wang, *Chin. Phys. B*, 2013, **22**, 066202.

15 R. Tang, Y. Li, S. Xie, N. Li, J. Chen, C. Gao, P. Zhu and X. Wang, *Sci. Rep.*, 2016, **6**, 38566.

16 A. Beltrán, L. Gracia and J. Andrés, *J. Phys. Chem. C*, 2019, **123**, 3239.

17 D. Díaz-Anichtchenko, D. Santamaría-Perez, T. Marqueño, J. Pellicer-Porres, J. Ruiz-Fuertes, R. Ribes, J. Ibáñez, S. N. Achary, C. Popescu and D. Errandonea, *J. Alloys Compd.*, 2020, **837**, 155505.

18 R. Tang, Y. Li, N. Li, D. Han, H. Li, Y. Zhao, C. Gao, P. Zhu and X. Wang, *J. Phys. Chem. C*, 2014, **118**, 10560.

19 S. Klotz, J. C. Chervin, P. Munsch and G. Le Marchand, *J. Phys. D: Appl. Phys.*, 2009, **42**, 7.

20 A. D. Chijioke, W. J. Nellis, A. Soldatov and I. F. Silvera, *J. Appl. Phys.*, 2005, **98**, 114905.

21 D. J. Higham and N. J. Higham, *MATLAB Guide*, Siam, 2016.

22 F. Fauth, I. Peral, C. Popescu and M. Knapp, *Powder Diffr.*, 2013, **28**, S360.

23 A. Dewaele, P. Loubeyre and M. Mezouar, *Phys. Rev. B: Condens. Matter Mater. Phys.*, 2004, **70**, 094112.

24 C. Prescher and V. B. Prakapenka, *High Pressure Res.*, 2015, **35**, 223.

25 W. Kraus and G. Nolze, *J. Appl. Crystallogr.*, 1996, **29**, 301.

26 P. Hohenberg and W. Kohn, *Phys. Rev.*, 1964, **136**, B864.

27 G. Kresse and J. Furthmüller, *Phys. Rev. B: Condens. Matter Mater. Phys.*, 1996, **54**, 86.

28 P. E. Blochl, *Phys. Rev. B: Condens. Matter Mater. Phys.*, 1994, **50**, 17953.

29 G. Kresse and D. Joubert, *Phys. Rev. B: Condens. Matter Mater. Phys.*, 1999, **59**, 1758.

30 A. E. Mattsson, R. Armiento, J. Paier, G. Kresse, J. M. Wills and T. R. Mattsson, *J. Chem. Phys.*, 2008, **128**, 084714.

31 R. Armiento and A. E. Mattsson, *Phys. Rev. B: Condens. Matter Mater. Phys.*, 2005, **72**, 085108.

32 H. J. Monkhorst and J. D. Pack, *Phys. Rev. B: Solid State*, 1976, **13**, 5188.

33 F. Birch, *Phys. Rev.*, 1947, **71**, 809.

34 A. Togo and I. Tanaka, *Scr. Mater.*, 2015, **108**, 1–5.

35 E. Kroumova, M. I. Aroyo, J. M. Perez-Mato, A. Kirov, C. Capillas, S. Ivantchev and H. Wondratschek, *Phil. Transit.*, 2003, **76**, 155.

36 J. Sánchez-Martín, J. Pellicer-Porres, A. Liang, J. Ibáñez, R. Oliva, C. Popescu, Z. He, P. Rodríguez-Hernández, A. Muñoz and D. Errandonea, *J. Phys. Chem. C*, 2023, **127**, 21684.

37 L. M. Uriarte, L. J. Bonales, J. Dubessy, A. Lobato, V. G. Baonza and M. Cáceres, *Microchem. J.*, 2018, **139**, 134.

38 D. Errandonea, E. Bandiello, A. Segura, J. J. Hamlin, M. B. Maple, P. Rodriguez-Hernandez and A. Muñoz, *J. Alloys Compd.*, 2014, **587**, 14.

39 V. Monteseguro, J. Ruiz-Fuertes, J. Contreras-García, P. Rodríguez-Hernández, A. Muñoz and D. Errandonea, *Appl. Phys. Lett.*, 2019, **115**, 012102.

40 D. Errandonea, D. Martínez-García, R. Lacomba-Perales, J. Ruiz-Fuertes and A. Segura, *Appl. Phys. Lett.*, 2006, **89**, 091913.

41 D. Errandonea, A. Muñoz and J. Gonzalez-Platas, *J. Appl. Phys.*, 2014, **115**, 216101.

42 A. Le Bail, H. Duroy and J. L. Fourquet, *Mater. Res. Bull.*, 1988, **23**, 447.

43 Y. Zou and H. Zhang, *J. Alloys Compd.*, 2019, **790**, 164.

44 B. Kalkan, B. K. Godwal, J. Yan and R. Jeanloz, *Phys. Rev. B*, 2022, **105**, 064111.

45 D. Errandonea, Y. Meng, M. Somayazulu and D. Häusermann, *Phys. Rev. B: Condens. Matter Mater. Phys.*, 2005, **355**, 116.

46 J. Zhao, R. J. Angel and N. L. Ross, *J. Appl. Crystallogr.*, 2010, **43**, 743.

47 J. Gonzalez-Platas, M. Alvaro, F. Nestola and R. Angel, *J. Appl. Crystallogr.*, 2016, **49**, 1377.

48 R. J. Angel, *Rev. Mineral. Geochem.*, 2000, **41**, 35.

49 H. Giefers and F. Porsch, *Phys. Rev. B: Condens. Matter Mater. Phys.*, 2007, **400**, 53.

50 J. Shanker, S. S. Kushwah and P. Kumar, *Phys. B*, 1997, **233**, 78.

51 C. Fan, Q. Wang, L. Li, S. Zhang, Y. Zhu, X. Zhang, M. Ma, R. Liu and W. Wang, *Appl. Phys. Lett.*, 2008, **92**, 101917.

52 M. Lertkiattrakul, M. L. Evans and M. J. Cliffe, *JOSS*, 2023, **8**, 5556.

53 F. Occelli, P. Loubeyre and R. Letoullec, *Nat. Mater*, 2003, **2**, 151.

54 D. Jiang, T. Wen, H. Song, Z. Jiang, C. Li, K. Liu, W. Yang, H. K. Mao and Y. Wang, *CCS Chem.*, 2022, **4**, 3246.

55 N. C. Burtch, J. Heinen, T. D. Bennett, D. Dubbeldam and M. D. Allendorf, *Adv. Mater.*, 2018, **30**, 1704124.

56 O. Gomis, B. Lavina, P. Rodríguez-Hernández, A. Muñoz, R. Errandonea, D. Errandonea and M. Bettinelli, *J. Phys.: Condens. Matter*, 2017, **29**, 095401.

57 D. Errandonea and A. B. Garg, *Prog. Mater. Sci.*, 2018, **97**, 123.

58 I. Loa, A. Grzechnik, U. Schwarz, K. Syassen, M. Hanfland and R. K. Kremer, *J. Alloys Compd.*, 2001, **317–318**, 103–108.

59 A. Liang, R. Turnbull and D. Errandonea, *Prog. Mater. Sci.*, 2023, **136**, 101092.

60 W. H. Baur, *Acta Crystallogr., Sect. B: Struct. Crystallogr. Cryst. Chem.*, 1974, **30**, 1195.